Lattice Boltzmann simulations of heat transfer in fully developed periodic incompressible flows

Zimeng Wang, Helen Shang, and Junfeng Zhang*
Bharti School of Engineering, Laurentian University, 935 Ramsey Lake Road, Sudbury, Ontario, Canada P3E 2C6
(Received 23 December 2016; revised manuscript received 5 March 2017; published 14 June 2017)

Flow and heat transfer in periodic structures are of great interest for many applications. In this paper, we carefully examine the periodic features of fully developed periodic incompressible thermal flows, and incorporate them in the lattice Boltzmann method (LBM) for flow and heat transfer simulations. Two numerical approaches, the distribution modification (DM) approach and the source term (ST) approach, are proposed; and they can both be used for periodic thermal flows with constant wall temperature (CWT) and surface heat flux boundary conditions. However, the DM approach might be more efficient, especially for CWT systems since the ST approach requires calculations of the streamwise temperature gradient at all lattice nodes. Several example simulations are conducted, including flows through flat and wavy channels and flows through a square array with circular cylinders. Results are compared to analytical solutions, previous studies, and our own LBM calculations using different simulation techniques (i.e., the one-module simulation vs. the two-module simulation, and the DM approach vs. the ST approach) with good agreement. These simple, however, representative simulations demonstrate the accuracy and usefulness of our proposed LBM methods for future thermal periodic flow simulations.

DOI: 10.1103/PhysRevE.95.063309

I. INTRODUCTION

Periodic structures are often encountered in heat exchangers and other heat transfer systems, such as wavy or grooved pipes, fin-pin cold plates, and cross-flow heat exchangers [1,2]. When fluid property changes are neglected, identical flow field and similar temperature distributions can be observed in consecutive periodic modules after some distance from the entrance. The flow is then called fully developed in both flow and thermal fields [3,4]. Numerous studies have been conducted on this topic; among them, existing simulations mainly used traditional numerical techniques such as the finite-difference and finite-volume methods [3–8].

Over the past two decades, the lattice Boltzmann method (LBM) has experienced significant development. In addition to various flow systems [9–13], LBM has also been successfully adopted to study other processes and phenomena, such as heat and mass transfer and electric and magnetic fields [14–16]. Unlike other traditional numerical schemes such as the finite-element, finite-difference, and finite-volume methods, where the governing equations of macroscopic properties are discretized mathematically, LBM works with a set of density distributions at each lattice node, and the evolution of these density distributions follows a simple collision-propagation process consecutively. Interestingly, macroscopic equations (such as the continuity and momentum equations for fluid dynamics, the convection-diffusion equation for heat and mass transfer, and the Poisson equation for electric fields) can be correctly recovered from the density distribution dynamics via mathematical analysis [14,15]. Studies and applications have shown that LBM has some advantages over other methods in simulating multiphase flows, incorporating complex boundary geometries and moving boundaries, and implementing for parallel computation.

To simulate thermal flow systems, several approaches have been developed along with the LBM advances over the past two decades. In general, these methods can be grouped in three categories: the multispeed approach, the double-distribution approach, and the hybrid approach [17,18]. The multispeed approach utilizes one set of distribution functions for both flow and thermal fields; however, additional lattice speeds and higher-order velocity terms are introduced to recover the macroscopic energy equation. While this approach may appear computationally attractive, its applications are relatively limited due to the severe numerical instability and the narrow temperature variation range [18]. The hybrid approach uses LBM only for the flow filed, and the energy equation is solved via some other traditional numerical schemes (e.g., the finite difference method); therefore the hybrid approach is not appropriate for our present work, since LBM is not involved in the thermal field solution at all. The double-distribution method employs two sets of distribution functions: one for the flow field and one for the thermal field. The double distribution method is most often used in thermal flow simulations, since the numerical stability is significantly improved compared to the multispeed method, and the computational implement is more convenient than the hybrid approach. For these concerns, we use the double-distribution approach in our next method description and simulation demonstration. More details on these thermal LBM models can be found in several review articles and books and references therein [14–17].

As with other numerical methods, appropriate boundary conditions are crucial for accurate and meaningful LBM simulations. At lattice nodes near the boundary, there are no density distributions entering the simulation domain after the propagation step, and therefore appropriate treatments must be implemented to assign values to such unknown density distributions such that the macroscopic boundary requirements are satisfied. Typically, macroscopic constraints on boundaries are available before simulations, such as the no-slip boundary condition on wall surfaces, the pressure values at the inlet and outlet, and the wall temperature or

*Corresponding author: jzhang@laurentian.ca

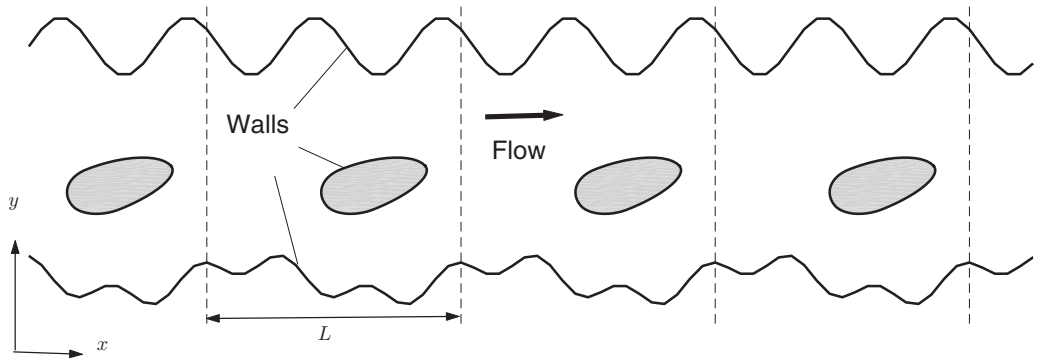

FIG. 1. Schematic illustration of the periodic flow passage. The vertical dashed lines are plotted to divide the flow passage into individual periodic modules. The coordinate system is set with the x direction in the flow direction and the y direction in the transverse direction.

heat flux in thermal systems. Tremendous efforts have been devoted to develop accurate and efficient boundary schemes for flow and thermal situations [14–17]. However, for the periodic thermal flow discussed in this paper, the exact velocity and temperature values at the module inlet and outlet cannot be specified, and those LBM boundary methods cannot be used. Fortunately, the particulate nature of LBM density distributions provides great convenience for applying periodic and symmetric (including the free-slip boundary condition in fluid flows and the adiabatic boundary condition in heat transfer) boundary conditions along a lattice grid line, which can be accomplished by simply recycling or reflecting the density distributions that cross the domain boundaries [15,16]. Both periodic and symmetric boundary treatments have been frequently used in LBM flow simulations [15,19–22]; however, this technical merit has not been recognized for LBM simulations of heat transfer processes in periodic incompressible flows yet.

In this paper, we extend the pressure periodic boundary method by Zhang and Kwok [19] to fully developed periodic incompressible thermal flows with constant wall temperature (CWT) or surface heat flux (SHF) boundaries. The similarity features of temperature field in periodic modules in such systems are first discussed. Two different numerical approaches, the distribution modification (DM) and the source term (ST) approaches, are developed to incorporate these similarity features in LBM simulations. At last, several validation and demonstration simulations are performed to illustrate the correctness, accuracy, and usefulness of our proposed methods in LBM simulations of periodic incompressible thermal flows.

II. THEORY AND METHODS

In this section we first describe in detail the periodic features of flow and temperature in fully developed periodic incompressible flows for both the CWT and SHF conditions. An outline of the LBM algorithm is included in Appendix A. Such information is well documented in the literature; and we represent these materials here for the completeness of this paper and for the convenience of the following discussions of our periodic boundary treatments.

A. Fully developed periodic thermal flows

Consider the two-dimensional (2D) system illustrated in Fig. 1 as a general example of the fully developed periodic flows driven under a pressure gradient. The flow and temperature fields are governed by the following continuity [Eq. (1)], momentum [Eq. (2)], and energy [Eq. (3)] equations:

$$\frac{\partial \rho}{\partial t} + \rho \nabla \cdot \mathbf{u} = 0, \tag{1}$$

$$\frac{\partial \mathbf{u}}{\partial t} + \nabla \cdot (\mathbf{u}\mathbf{u}) = -\frac{\nabla P}{\rho} + \nu \nabla^2 \mathbf{u}, \tag{2}$$

$$\frac{\partial T}{\partial t} + \mathbf{u} \cdot \nabla T = \alpha \nabla^2 T, \tag{3}$$

where $\mathbf{u}$ is the flow velocity, P is the pressure, T is the temperature, ρ is the fluid density, ν is the kinematic fluid viscosity, α is the fluid thermal diffusivity, and t is time. Here we have neglected the viscous dissipation term in the energy equation as in typically heat transfer research. When the flow is fully developed along the periodic passage, the velocity $\mathbf{u}$ becomes identical at locations of the same relative position in each periodic module (we will call them image locations hereafter) [3,6], i.e.,

$$\mathbf{u}(x \pm mL, y) = \mathbf{u}(x, y), \tag{4}$$

where L is the streamwise length of the periodic unit and m is a natural number. The fluid pressure keeps decreasing along the flow direction; however, the following relationship exists among image locations:

$$P(x \pm mL, y) = P(x, y) \mp m\Delta P_L, \tag{5}$$

and the pressure drop over each periodic unit ΔP_L remains constant. It is easy to verify that $\mathbf{u}(x \pm mL, y)$ and $P(x \pm mL, y)$ are still valid solutions of the continuity and momentum Eqs. (1) and (2), since the identical velocity and shifted pressure cause no change to any terms in these governing differential equations. Meanwhile, the no-slip boundary condition, if satisfied in one unit, will also be satisfied in all other units. To obtain an exact periodic boundary condition for pressure like Eq. (4) for velocity, Patankar *et al.* [3] split the fluid pressure P into two components: a global pressure term $-\Delta P_L x/L$ and a local reduced pressure $\widetilde{P}$:

$$P(x, y) = -\frac{\Delta P_L}{L} x + \widetilde{P}(x, y). \tag{6}$$

After this modification, the momentum Eq. (2) is rewritten to

$$\frac{\partial \mathbf{u}}{\partial t} + \nabla \cdot (\mathbf{uu}) = -\frac{\nabla \widetilde{P}}{\rho} + \nu \nabla^2 \mathbf{u} + \frac{\Delta P_L}{\rho L}, \tag{7}$$

and Eq. (5) now changes to a perfect periodic boundary condition:

$$\widetilde{P}(x \pm mL, y) = \widetilde{P}(x, y). \tag{8}$$

As for the temperature field, the periodic features depend on the boundary conditions imposed on the walls. For fully developed periodic thermal flows to be established, the solid surfaces must have a uniform, constant wall temperature (CWT) T_w, or they can have specified surface heat flux (SHF). For the latter situation, the heat flux could be uniform or varying over the surface within one module, but it must have the same distribution for all units. For the CWT systems, usually we first shift the temperature field by the wall temperature T_w to a reduced temperature θ

$$\theta(x, y) = T(x, y) - T_w, \tag{9}$$

and the energy Eq. (3) becomes

$$\frac{\partial \theta}{\partial t} + \mathbf{u} \cdot \nabla \theta = \alpha \nabla^2 \theta; \tag{10}$$

with the wall boundary condition for θ as $\theta(\Omega) = 0$ (here Ω denotes the wall surface). The periodic relationship for θ among modules is expressed as

$$\theta(x \pm mL, y) = e^{-\lambda_L (\pm mL)} \theta(x, y), \tag{11}$$

where λ_L is the decaying rate that describes the overall temperature variation in the streamwise direction [6]. Similar to the flow velocity and pressure discussed above, one can see that, if $\theta(x, y)$ is a valid solution in one unit, $\theta(x \pm mL, y)$ from the above equation will automatically satisfy the energy Eq. (10) in other units. Stalio and Piller [6] then introduced a normalized temperature $\bar{\theta}(x, y)$ as

$$\bar{\theta}(x, y) = \frac{\theta(x, y)}{e^{-\lambda_L x}} = \frac{T(x, y) - T_w}{e^{-\lambda_L x}}. \tag{12}$$

As a result, the energy equation for $\bar{\theta}$ is

$$\frac{\partial \bar{\theta}}{\partial t} + \mathbf{u} \cdot \nabla \bar{\theta} = \alpha \nabla^2 \bar{\theta} + \left(\alpha \lambda_L^2 + \lambda_L u_x\right) \bar{\theta} - 2\alpha \lambda_L \frac{\partial \bar{\theta}}{\partial x} \tag{13}$$

with an exact periodic boundary condition

$$\bar{\theta}(x \pm mL, y) = \bar{\theta}(x, y). \tag{14}$$

In Eq. (13), u_x represents the x component of the flow velocity vector $\mathbf{u}$.

To determine the decaying rate λ_L, Stalio and Piller [6] integrated the energy Eq. (13) and obtained λ_L as the root of a quadratic equation. Here we propose another simpler approach to find λ_L by considering the energy conservation over a periodic module. Taking the fluid volume in a periodic unit as the control volume, there are five streams of heat fluxes crossing the control volume boundaries (including the walls and the inlet and outlet of the periodic unit):

(i) heat flux entering the control volume with flow at the inlet: $\rho c \int_{in} u_{x,in} \theta_{in} dy$;

(ii) heat flux leaving the control volume with flow at the outlet: $\rho c \int_{out} u_{x,out} \theta_{out} dy$;

(iii) streamwise diffusion flux leaving the control volume at the inlet: $\kappa \int_{in} \left(\frac{\partial \theta}{\partial x}\right)_{in} dy$;

(iv) streamwise diffusion flux entering the control volume at the outlet: $\kappa \int_{out} \left(\frac{\partial \theta}{\partial x}\right)_{out} dy$;

(v) heat flux leaving the control volume over the wall surface Ω: $\kappa \int_{\Omega} \left(\frac{\partial \theta}{\partial n}\right)_{\Omega} ds$.

According to the energy conservation principle, for a steady system we have:

$$\rho c \int_{in} u_{x,in} \theta_{in} dy - \rho c \int_{out} u_{x,out} \theta_{out} dy - \kappa \int_{in} \left(\frac{\partial \theta}{\partial x}\right)_{in} dy + \kappa \int_{out} \left(\frac{\partial \theta}{\partial x}\right)_{out} dy - \kappa \int_{\Omega} \left(\frac{\partial \theta}{\partial n}\right)_{\Omega} ds = 0. \tag{15}$$

Here we use the subscripts in and out to indicate the inlet and outlet locations, and n for the local normal direction on the wall surface. c is the heat capacity and κ is the thermal conductivity of the fluid. Now applying the periodic relationships in Eqs. (4) for velocity $\mathbf{u}$ and (11) for T, the decaying rate λ_L can be solved as

$$\lambda_L = -\frac{1}{L} \ln \left[1 - \frac{\alpha \int_{\Omega} \left(\frac{\partial \theta}{\partial n}\right) ds}{\int_{in} \left(u_x \theta + \alpha \frac{\partial \theta}{\partial x}\right)_{in} dy}\right]. \tag{16}$$

Compared to the calculation method in Ref. [6], our method does not require volumetric integration over the entire simulation domain, which could be computational expensive especially in three-dimensional simulations.

Now we turn our attention to the SHF systems. In this situation, the periodic relationship for temperature is given as

$$T(x \pm mL, y) = T(x, y) \pm m \Delta T_L, \tag{17}$$

which is similar to that for the normal fluid pressure P in Eq. (5). Here ΔT_L is the temperature change over a periodic unit and it is constant along the flow. Accordingly, Patankar *et al.* [3] defined a reduced temperature $\widetilde{T}$ as

$$\widetilde{T}(x, y) = T(x, y) - \frac{\Delta T_L}{L} x \tag{18}$$

to achieve a perfect periodic boundary condition for $\widetilde{T}$:

$$\widetilde{T}(x \pm mL, y) = \widetilde{T}(x, y); \tag{19}$$

and the energy equation should be rewritten correspondingly to

$$\frac{\partial \widetilde{T}}{\partial t} + \mathbf{u} \cdot \nabla \widetilde{T} = \alpha \nabla^2 \widetilde{T} - \frac{u_x \Delta T_L}{L}. \tag{20}$$

The temperature change ΔT_L can be relatively easily found from the energy conservation principle:

$$\Delta T_L = \frac{\int_{\Omega} q ds}{\rho c \int_{in} u_{x,in} dy}, \tag{21}$$

i.e., the temperature change equals the total thermal energy addition via the surface divided by the product of flow rate and volumetric heat capacity (ρc). Here q is the local heat flux entering the fluid domain via the boundary walls.

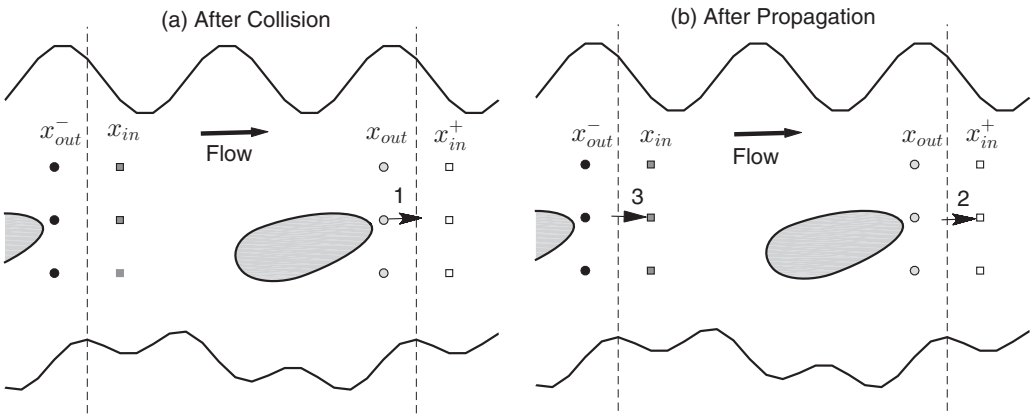

FIG. 2. Schematic illustrations of the modified periodic boundary treatment for thermal field. The inlet nodes are displayed as squares and the outlet nodes are shown as circles, with the color changing from black to white along the flow direction. The numbered arrows are used to show how a density distribution leaving the outlet can be adopted to specify the incoming distribution at the inlet. Please refer the text for detailed method description.

B. Simulating periodic thermal flows with LBM

In LBM, governing equations are solved by means of density distributions, which undergo consecutive propagation and collision processes over a lattice grid. In the work, we use the double-distribution thermal LBM scheme for method descriptions and simulation demonstration. The two-dimensional, nine-velocity (D2Q9) lattice structure and the single-relaxation Bhatnagar-Gross-Krook (BGK) model are used for both flow and thermal fields. Please refer to Appendix A for details.

1. For flow field

Under a given pressure drop ΔP_L per periodic module, it is convenient to use the reduced pressure $\widetilde{P}$ defined in Eq. (6), and the LBM equations for f_i given in Appendix A can then be used $\mathbf{F} = (\Delta P_L/\rho L, 0)^T$. The classical periodic boundary condition [16] can then be applied at the periodic boundaries, meaning density distributions leaving the domain outlet will reenter the domain at the inlet, or vice versa. This method has been widely used in LBM simulations, although more dedicate treatments are available to impose the pressure drop directly for some particular situations like multiphase or multicomponent flows [19]. To simulate a periodic flow with a specific flow rate, the pressure drop ΔP_L can be dynamically adjusted according to the simultaneous flow rate till the desirable value is established.

2. For thermal field: The source term (ST) approach

Similarly, by tuning the source term δh_i according to Eq. (A13), the LBM algorithm for h_i in Appendix A can be used to solve Eq. (13) for CWT systems

$$\delta h_i = \omega_i \left[\left(\alpha\lambda_L^2 + \lambda_L u_x\right)\bar{\theta} - 2\alpha\lambda_L \frac{\partial\bar{\theta}}{\partial x} \right] \tag{22}$$

for energy scalar $A = \bar{\theta}$; or to solve Eq. (20) for SHF cases with

$$\delta h_i = \omega_i \left[-\frac{u_x \Delta T_L}{L} \right] \tag{23}$$

for energy scalar $A = \widetilde{T}$. The temperature change ΔT_L for SHF cases can be readily calculated from the total heat flux over surface via Eq. (21); however, for CWT systems, the decaying rate λ_L is unknown before the simulation. In our practice, we start with an initial guess and run the simulation for some time (2000 time steps in our simulations) with that initial value. After that, a new λ_L value is calculated via Eq. (16) every certain time steps (we use 20 time steps), till the simulation becomes steady in flow and temperature fields. The differential term $\partial\bar{\theta}/\partial x$ in Eq. (13) can be estimated by a finite difference approximation.

3. For thermal field: The distribution modification (DM) approach

Another way to incorporate the periodic features of the temperature field described in Sec. II A is to modify those density distributions h_i that cross the module inlet or outlet boundaries, as done in Ref. [19] for pressure periodic boundary conditions. We consider the CWT situation in the periodic system shown in Fig. 1, and enlarge one module in Fig. 2 with the first column of lattice nodes at x_{in} (dark gray squares) and the last column at x_{out} (light gray circles). Also displayed are the outlet nodes of the upstream module at $x_{out}^- = x_{in} - \delta x = x_{out} - L$ (black circles) and the inlet nodes of the downstream module at $x_{in}^+ = x_{in} + L = x_{out} + \delta x$ as (white squares); although these nodes are actually not involved in the LBM calculation. To avoid the extra source term in Eq. (13), we will use LBM to solve the energy Eq. (10) for θ. Now let us take the postcollision distribution $h_1^*(x_{out})$ at x_{out} [Arrow 1 in Fig. 2(a)] as an example. In the propagation step, $h_1^*(x_{out})$ is supposed to move to the next node in velocity $\mathbf{c}_1 = (1,0)^T$, and becomes the incoming distribution at the inlet node of the downstream module x_{in}^+ [Arrow 2 in Fig. 2(b)]. However, now it is out of our simulation domain and therefore cannot participate in the LBM calculation anymore. On the other side, we need the incoming distribution $h_1(x_{in})$ at the domain inlet x_{in} [Arrow 3 in Fig. 2(b)], but it is not available since the nodes at the x_{out}^- are not in the simulation domain either. Based on the periodic relationship of temperature given in Eq. (11) and $\theta = \sum_i h_i$ [Eq. (A3) with $A = \theta$], it is reasonable to assume the proportionality in θ can be extended

to each distribution h_i, and therefore one has

$$h_1(x_{in},t+\delta t) = e^{\lambda_L L} h_1(x_{in}^+,t+\delta t) = e^{\lambda_L L} h_1^*(x_{out},t). \quad (24)$$

This analysis can be extended to other lattice distributions that cross the periodic boundaries during the propagation step, and a modified periodic boundary treatment for these distributions can be established as (for the D2Q9 lattice model used here)

$$h_i(x_{in},y_{in},t+\delta t) = e^{\lambda_L L} h_i^*(x_{out},y_{out},t), \quad y_{in} = y_{out} + c_{i,y}\delta t, \quad i = 1,5,8; \quad (25)$$

$$h_i(x_{out},y_{out},t+\delta t) = e^{-\lambda_L L} h_i^*(x_{in},y_{in},t), \quad y_{out} = y_{in} + c_{i,y}\delta t, \quad i = 3,6,7. \quad (26)$$

Here $c_{i,y}$ is the y component of the lattice velocity $\mathbf{c}_i$.

This distribution modification (DM) approach is also applicable to the SFH cases. Here we work with the original energy Eq. (3) and rewrite the periodic relationship for the regular temperature T Eq. (17) to define a proportional factor β as

$$\beta = \frac{T(x_{in}^+)}{T(x_{in})} = 1 + \frac{\Delta T_L}{T(x_{in})}; \quad (27)$$

and, following the above discussion, the modified periodic boundary condition for h_i in SHF systems is

$$h_i(x_{in},y_{in},t+\delta t) = \beta^{-1} h_i^*(x_{out},y_{out},t), \quad y_{in} = y_{out} + c_{i,y}\delta t, \quad i = 1,5,8; \quad (28)$$

$$h_i(x_{out},y_{out},t+\delta t) = \beta h_i^*(x_{in},y_{in},t), \quad y_{out} = y_{in} + c_{i,y}\delta t, \quad i = 3,6,7. \quad (29)$$

Note these modified periodic treatments revert back to the classical periodic boundary condition in LBM when the proportional factor $e^{-\lambda_L}$ or β is set to 1.

III. VALIDATION AND DEMONSTRATION SIMULATIONS

In this section, we apply the periodic treatments described above to simulate the flow and temperature fields in several simple, however, representative and carefully designed periodic systems, including flows through a flat channel, a wavy channel, and a square array of circular cylinders. Both CWT and SHF boundary conditions are considered, and results are compared with available analytical solutions, previous publications, or our own LBM results using different simulation techniques (DM vs ST approaches and one-module vs two-module domain simulations).

A. Heat transfer of laminar flow through 2D flat channel

The fully developed flow in a uniform pipe or channel can be considered as an extreme example of periodic flows, for which the periodic module can be selected as a segment of the channel of any finite length. Here our simulation domain is a 2D rectangle of length $L = 100$ and height $H = 50$ (both L and H, as well as other LBM parameters to be given in this section, are all nondimensional values). The midpoint boundary method recently developed by Zhang and coworkers [18,23,24] is implemented at the solid-fluid boundaries for both flow and thermal LBM calculations for all simulations in this paper. The Reynolds number $\mathrm{Re} = U_0 H/\nu$ is 40, with the mean flow velocity U_0 defined as

$$U_0 = \frac{1}{H}\int_0^H u_x dy. \quad (30)$$

The Prandlt number $\mathrm{Pr} = \nu/\alpha$ is 0.7. The CWT situation is considered here and wall temperature T_w is set as 0; thus the regular temperature T and the reduced temperature θ are the same. During the simulation, the mean flow temperature at the domain inlet $T_0 = T_m(x = 0)$ is maintained at 1. Brown [25] had developed an analytical solution in polynomial series for thermal flows between parallel plates with constant temperature, however, with the axial diffusion neglected. In Appendix B, we extend the Brown solution to include the axial diffusion effect. Figure 3 shows the comparison between

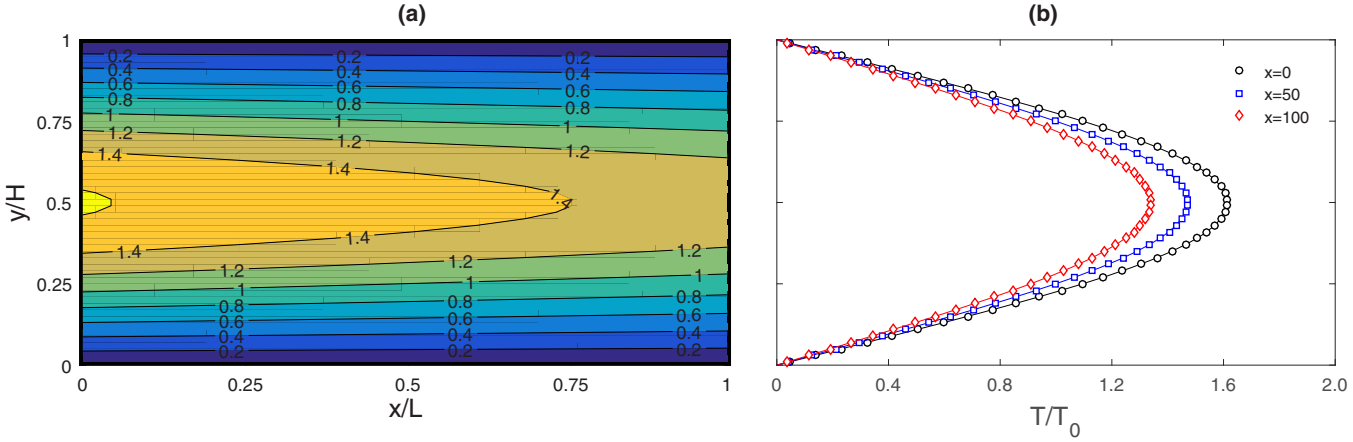

FIG. 3. (a) The simulated temperature field and (b) transverse profiles for flow through the flat channel with CWT condition on the channel surfaces. In (b) the symbols are our LBM results and the underlying curves are from the analytical solution in Appendix B.

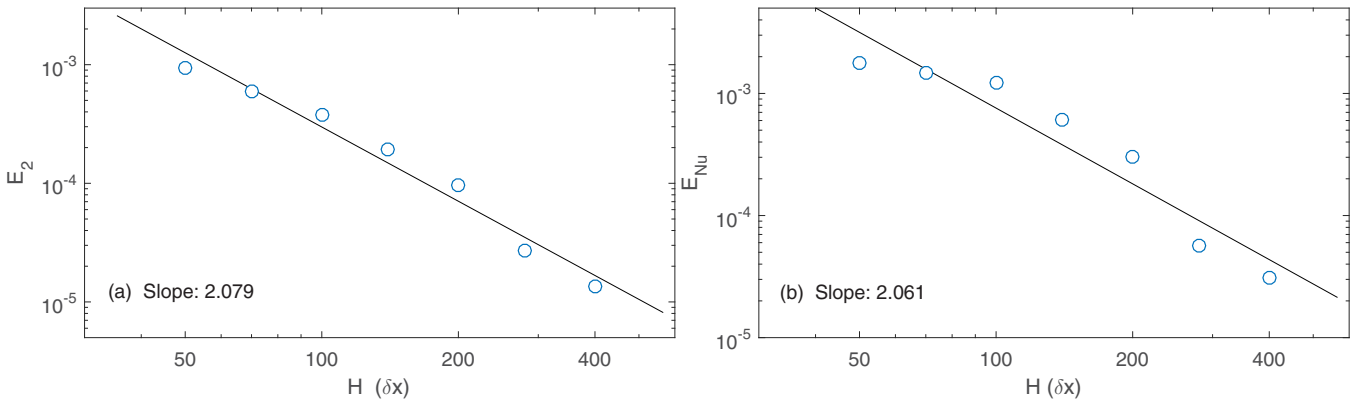

FIG. 4. The relative errors (a) E_2 and (b) E_{Nu} for flows through CWT flat channels with different channel height H. The straight lines are liner fittings of the LBM data points (symbols) in the log-log plots, and the line slopes are displayed in the figure labels.

our LBM results using the DM periodic boundary method and those from our analytical solution (see Appendix B) for the temperature field. No visible discrepancy can be observed. According to our analytical solution the Nusselt number along the channel is constant at 3.7723; while our LBM yields a range of 3.7736 ± 0.0065 (mean $\pm$ SD) along the channel. The relative difference is only $-0.14 \sim 0.21\%$. This small difference could be from several sources, including the basic LBM algorithm [14,15,26], the simple force term treatment in Eq. (A12) [17], the finite-difference approximations involved in our calculation, as well as the boundary methods [27]. Further investigations for the individual contributions from different aspects (and they are very likely intercoupled) is out of the scope of this paper.

For a more quantitative assessment of the numerical accuracy, we simulate the above system using different channel height H with the length-height ratio constant at $L/H = 2$. The global relative error E_2 is defined as

$$E_2 = \left[\frac{\sum (T_{LBM} - T_{th})^2}{\sum T_{th}^2}\right]^{1/2}, \tag{31}$$

where both summations are carried out over all lattice nodes in the simulated domain. The subscripts LBM and th are used to indicate, respectively, the LBM calculated temperature values and theoretical values from the analytical solution given in Appendix B. In addition, the local Nusselt number for this system can be calculated from the temperature filed by

$$\mathrm{Nu}(x) = \frac{(\partial T/\partial n)_{y=0} H}{T_m(x) - T_w}, \tag{32}$$

where T_m is the local mean flow temperature

$$T_m(x) = \frac{\int_0^H u_x(x,y) T(x,y) dy}{\int_0^H u_x(x,y) dy}. \tag{33}$$

The relative error with respect to this theoretical Nusselt number Nu_{th} has also be defined as

$$E_{\mathrm{Nu}} = \left[\frac{\sum (\mathrm{Nu}_{LBM} - \mathrm{Nu}_{th})^2}{\sum \mathrm{Nu}_{th}^2}\right]^{1/2}. \tag{34}$$

Here the summations are performed along the two boundary walls, and $\mathrm{Nu}_{th} = 3.7723$ from our analytical solution. These relative errors at different channel height H are plotted in Fig. 4 in the log-log scale. Clearly the relative errors decrease with the channel height H, and the declining slopes in the log-log graphs are approximately 2, which is similar to previous observations of other LBM models [14,17].

B. Heat transfer of laminar flow through 2D wavy channel

The flow and heat transfer through wavy channels have been extensively investigated for its practical applications [5,6,8,28,29]. Here we consider the same geometry as in these studies, and model the symmetric wavy wall shape by

$$H(x) = H_{\mathrm{avg}} - 2a \cos\left(\frac{2\pi x}{L}\right), \tag{35}$$

where $H(x)$ is the local channel width, H_{avg} is the average channel width over a periodic unit, and a is the wavy amplitude. The maximum channel width $H_{\max} = H_{\mathrm{avg}} + 2a$ occurs at the middle $x = L/2$ and the minimum width $H_{\min} = H_{\mathrm{avg}} - 2a$ occurs at the inlet $x = 0$ and outlet $x = L$. Following those previous studies, we use $H_{\mathrm{avg}}/L = 13/28$ and $a/L = 1/8$. The computational domain length here is $L = 240$. As in the flat channel simulation, we have $T_w = 0$, $T_0 = 1$, and $\mathrm{Pr} = 0.7$; and the DM method is used to incorporate the boundary periodicity. The Reynolds number is defined as $\mathrm{Re} = U_0 H_{\mathrm{avg}}/\nu$ [8,28], and two values, $\mathrm{Re} = 25$ and 100, are tested in our simulations.

Figure 5 collects our LBM results of these two calculations, including the flow streamlines, the isotherms, and the spanwise profiles of streamwise velocity u_x and temperature T at the maximum and minimum width locations. The streamline and isotherm patterns are very similar to those reported in previous studies [8,28]; however, a direct comparison is difficult due to the lack of original data for those publications and analytical solutions of this system. At $\mathrm{Re} = 100$, a pair of circulation vortex have developed in the wide section, and the separation and reattachment locations are similar to those in Ref. [8]. In Fig. 6, we also plot the distribution profiles of the normalized wall vorticity ζ_w [29]

$$\zeta_w = \frac{1}{2}\mathrm{Re} C_f \left(\frac{H_{\max}}{H_{\mathrm{avg}}}\right)^2 = \frac{1}{2}\mathrm{Re}\frac{\tau_w}{\rho U_0^2/2}\left(\frac{H_{\max}}{H_{\mathrm{avg}}}\right)^2 \tag{36}$$

and the local Nusselt number Nu. Here C_f is the local frictional coefficient and τ_w is the wall shear stress. These distribution

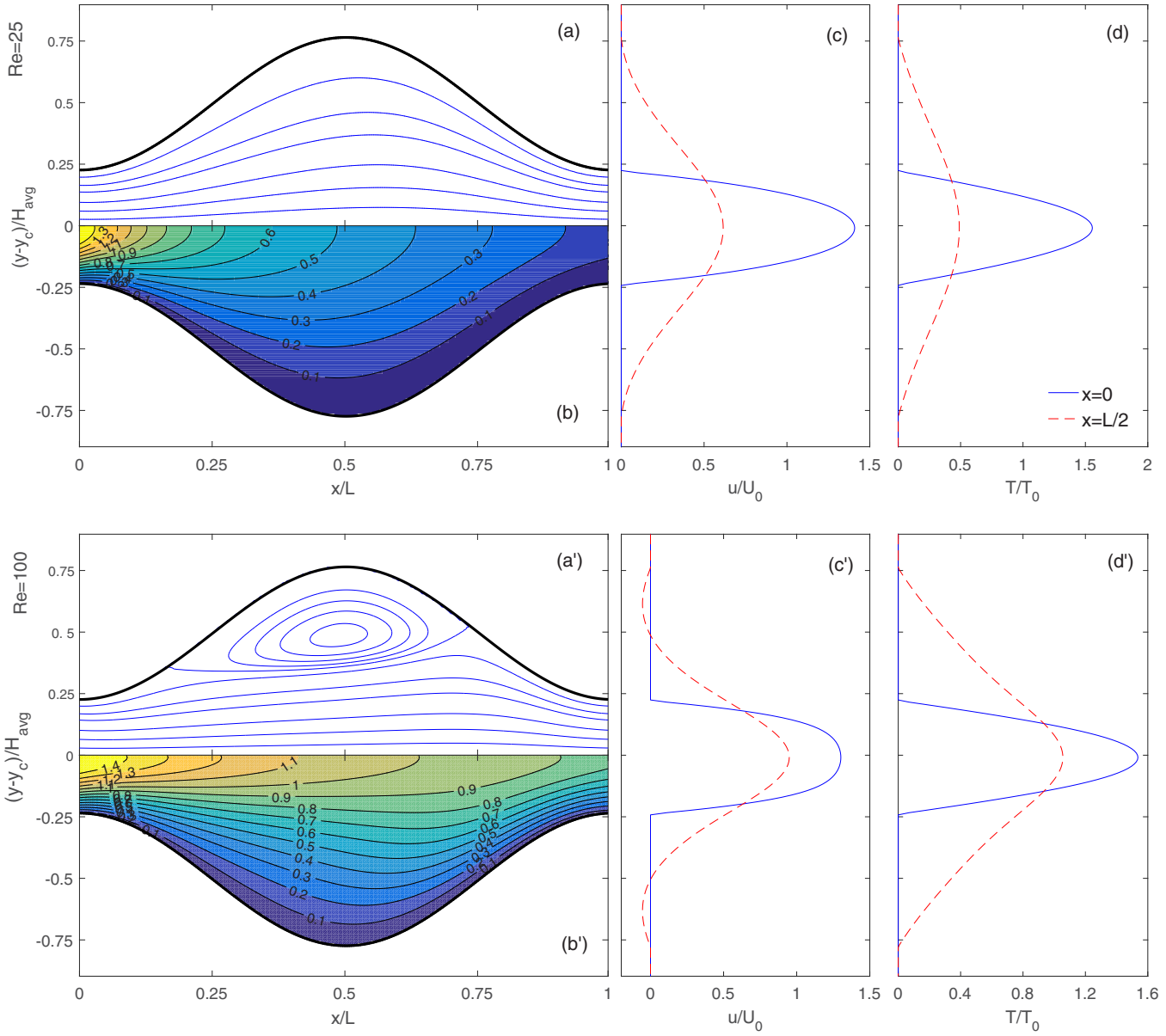

FIG. 5. [(a) and (a′)] The simulated flow and [(b) and (b′)] temperature fields and transverse velocity and temperature profiles [(c) and (c′)] for the streamwise velocity; and [(d) and (d′)] for the temperature) at two locations $x = 0$ and $x = L/2$ for the flows through a wavy channel with Reynolds number Re $= 25$ [(a)–(d)] and Re $= 100$ [(a′)–(d′)].

profiles are very similar to those reported in Ref. [29], both in the variation trend and magnitude. More quantitatively, we manually measure the velocity values u_x^c at the domain center $(L/2, y_c)$ (y_c is the y location of the channel centerline) from figures in Refs. [8,28], and compare them to ours in Table I. In addition, we have also calculated the friction factor f

$$f = \frac{\Delta P_L}{\rho U_0^2/2}\frac{H_{\rm avg}}{L} \tag{37}$$

and average Nusselt number $\langle \mathrm{Nu} \rangle$ for a periodic module [5,8]

$$\langle \mathrm{Nu} \rangle = \frac{[T_m(0) - T_m(L)]\int_{in} u_x dy}{\Delta}\frac{H_{\rm avg}}{\alpha}, \tag{38}$$

where Δ is the log-mean temperature difference in the module

$$\Delta = \frac{T_m(0) - T_m(L)}{\ln[T_m(L)/T_m(0)]}. \tag{39}$$

These values are also listed in Table I in comparisons with those from previous studies. It can be seen there that our results, including the domain center velocity, friction factor, and average Nusselt number, all agree well to previous publications. As discussed in Ref. [28], the discrepancy among these studies might be due to the different numerical methods employed.

C. Heat transfer in flow through square cylinder array

The last system we simulate represents the heat transfer process associated to laminar flow through a square array of

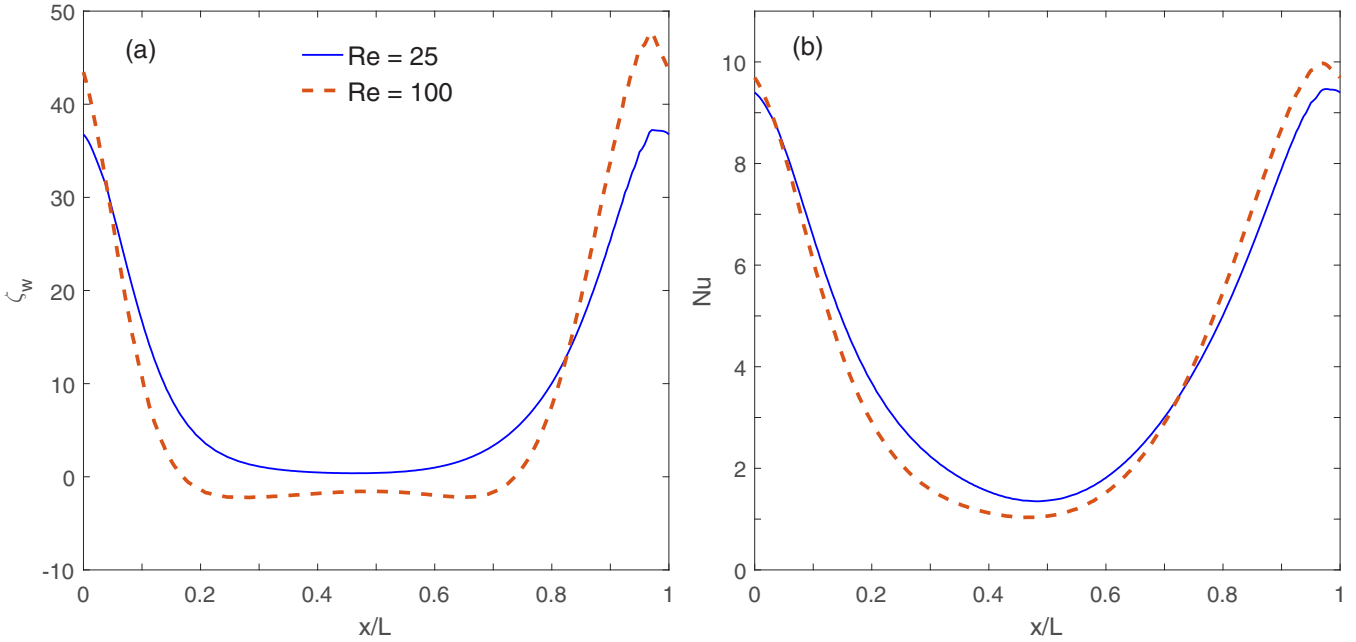

FIG. 6. Distributions of (a) the normalized wall vortex ζ_w and (b) local Nusselt number Nu along the channel wall.

circular cylinders, which resembles the interior configuration of a cross-flow tube heat exchanger [1,2]. The periodic module here is a square with $L = H = 160$, and the cylinder has a diameter of $D = 40$ and its center locates at $(3L/8, L/2)$. The flow direction is from the left to the right in the x direction, and the regular periodic boundary condition is applied along the top and bottom edges. The Reynolds number $\mathrm{Re} = U_0 H/\nu = 2.4$ and the Prandlt number $\mathrm{Pr} = 1$.

For a fully developed periodic incompressible flow, if the periodic relationships are physically correct and they have been accurately implemented in a numerical model, using one or two or even multiple periodic modules as the simulation domain should generate the same results. To confirm this statement, we perform two separate simulations for the above described cylinder array system: the first one includes one module with a square simulation domain of $L \times L$, and the second one includes two modules with a rectangular domain of $2L \times L$ and it has two cylinders: one at $(3/8L, L/2)$ and another at $(11/8L, L/2)$. The cylinder surface temperature $T_w = 0$ and inflow average temperature $T_0 = 1$. No analytical solutions are available for this system. Comparison of these two sets of results is displayed in Fig. 7. Please note that in Fig. 7(a) for the temperature field, the color patches are from the two-module simulation while the isotherm lines are from the one-module calculation. Clearly they agree to each other excellently and the isotherm lines follow the color patch edges exactly. More quantitatively, in Fig. 7(b), we plot the temperature profiles at several representative streamwise locations, and we see those at $x/L = 0$ and $3/8$ from the two simulations match each other perfectly. The difference in temperature in the first module from these two calculations is of the order $10^{-6} \sim 10^{-5}$. We also plot the temperature profiles at corresponding locations in the second module (i.e., $x/L = 1$ and $11/8$) from the two-module simulation, and we can clearly see the proportional similarity in variation as expressed in Eq. (11). Actually the profiles at $x/L = 1$ and $11/8$ scaled up by $e^{\lambda_L L}$ ($\lambda_L = 3.885233 \times 10^{-3}$ from the one-module simulation and $\lambda_L = 3.885264 \times 10^{-3}$ from the two-module simulation; they are almost identical) are also plotted in the figure; however, they are visually indistinguishable from the profiles at $x/L = 0$ and $3/8$, respectively.

A more direct comparison of the temperature fields from these two simulations is presented in Fig. 8. The magnitude of temperature difference, from the two different simulations, or between the left and right sections of the same two-module simulation, is of the order of $10^{-6} \sim 10^{-5}$. With the inlet mean temperature of 1 in these simulations, this difference can be considered as the relative errors as well. The patterns in Figs. 8(a) and 8(b) appear interesting; however, it is difficult for the authors to explore the underlying mechanisms due the system complexity. With this comparison, it is further confirmed that the periodic features have been

TABLE I. Comparison of the center velocity u_x^c, friction factor f and Nusselt number Nu from our LBM simulations to those from previous publications. The data of Ref. [5] are approximated using linear interpolation or extrapolation based on the converted values from Ref. [28].

	Center Velocity u_x^c			Friction Factor f				Nusselt Number Nu			
Re	Ref. [28]	Ref. [8]	this work	Ref. [28]	Ref. [8]	Ref. [5]	this work	Ref. [28]	Ref. [8]	Ref. [5]	this work
25	0.619	0.596	0.620	1.483	1.294	1.871	1.469	4.39	4.39	3.94	4.395
100	0.955	0.929	0.949	0.458	0.415	0.725	0.455	4.27	4.59	4.03	4.559

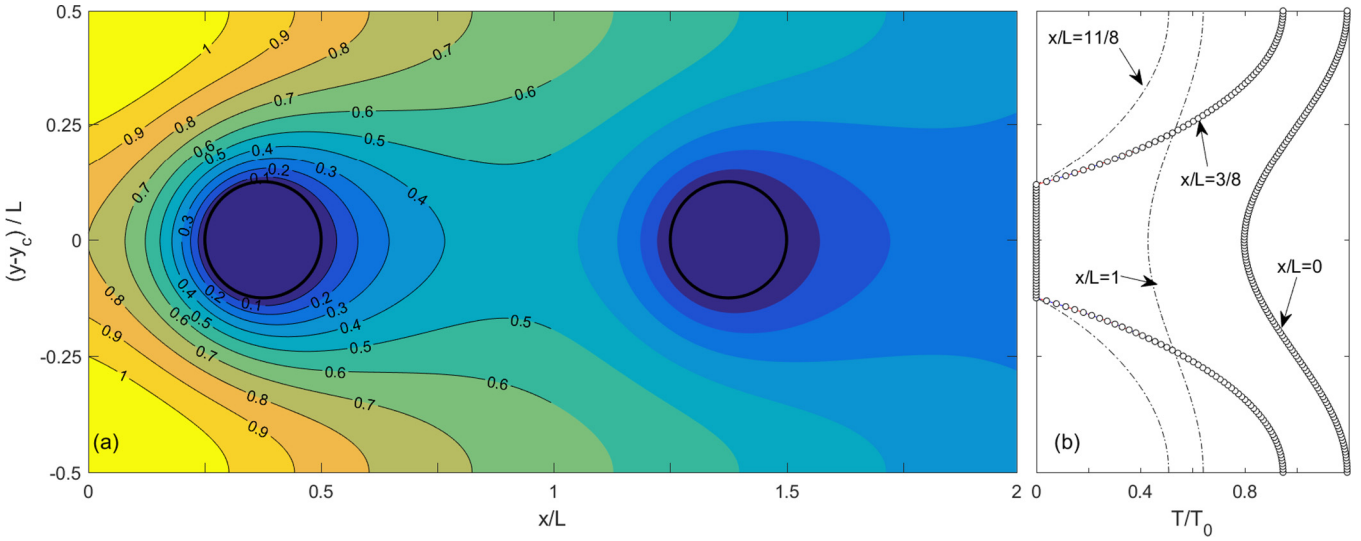

FIG. 7. Result comparison of the simulations for the cooling process of flow around cylinder with one or two modules included in the simulation domain. In (a) for the temperature field, the color patches are from the two-module simulation, and the isotherm lines are from the one-module simulation. The temperature profiles at $x/L = 0$, 3/8, 1, and 11/8 (indicated by labels) are displayed in (b), with the symbols from the one-module calculation and curves from the two-module calculation.

correctly and accurately implemented in our method and program.

So far all our simulations are for the CWT boundary condition and only the DM approach has been used. At last, we test the SHF boundary condition and the ST approach using the same cylinder array geometry. Four individual simulations are conducted: CWT+DM (the same one-module simulation described above), CWT+ST, SHF+DM, and SHF+ST. To impose a desirable heat flux (i.e., normal temperature gradient) on the surface, the Neumann boundary method developed by Oulaid *et al.* [30] is employed. With the inlet mean temperature $T_0 = 1$ and wall temperature $T_w = 0$, the CWT case represents a cooling process. On the other hand, for SHF case, we use a uniform surface flux with $\partial T/\partial n = -0.01$ for the cylinder surface and it therefore is a heating process. Results from these simulations, including the temperature field in the domain and two representative transverse temperature profiles, are collected in Fig. 9. The cooling or heating effect from the cylinder is clearly indicated by the isotherms in Figs. 9(a) and 9(a′), respectively. It is interesting to see that, in Fig. 9(a′) for the SHF boundary situation, the temperature increases along the centerline near the outlet. This is understandable since the outlet is close to the heating source (the cylinder) in the next module, and for this diffusion-dominant system (Peclet number $\mathrm{Pe} = \mathrm{RePr} = 2.4$), the heating flux from the next cylinder can reach a relatively long distance even against the flow direction. As for the results from the DM or ST approaches for both CWT and SHF boundary conditions, one can see again excellent agreement exists in Fig. 9, and no apparent difference can be spotted. The decaying rate λ_L value is 3.88554×10^{-3} from the DM approach, and 3.88533×10^{-3} from the ST approach. Such a nearly perfect match indicates that both the DM and ST approaches can produce reliable results for simulating developed periodic thermal flows.

A similar comparison is performed in Fig. 10, which displays the distributions over the simulation domain between the ST and DM simulations with CWT [Figs. 10(a) and 10(b)] and SHF [Figs. 10(a) and 10(b)] wall conditions. Again the difference magnitude is relatively small ($10^{-6} \sim 10^{-5}$), suggesting that both the DM and ST methods can be

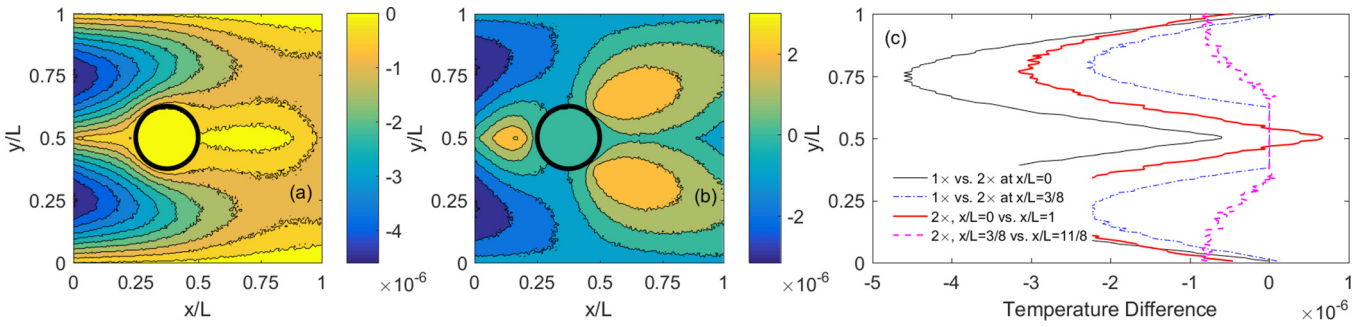

FIG. 8. Distributions of temperature difference (a) in the left $L\times L$ domain between the one-module and two-module simulations, and (b) that between the left ($x \in [0,L]$) and right ($x \in [L,2L]$) half domain from the two-module simulation. In (b) the temperature in the right half domain has been scaled up by a factor of $e^{\lambda_L L}$ for direct comparison. (c) shows the temperature difference from (a) and (b) at two representative x locations.

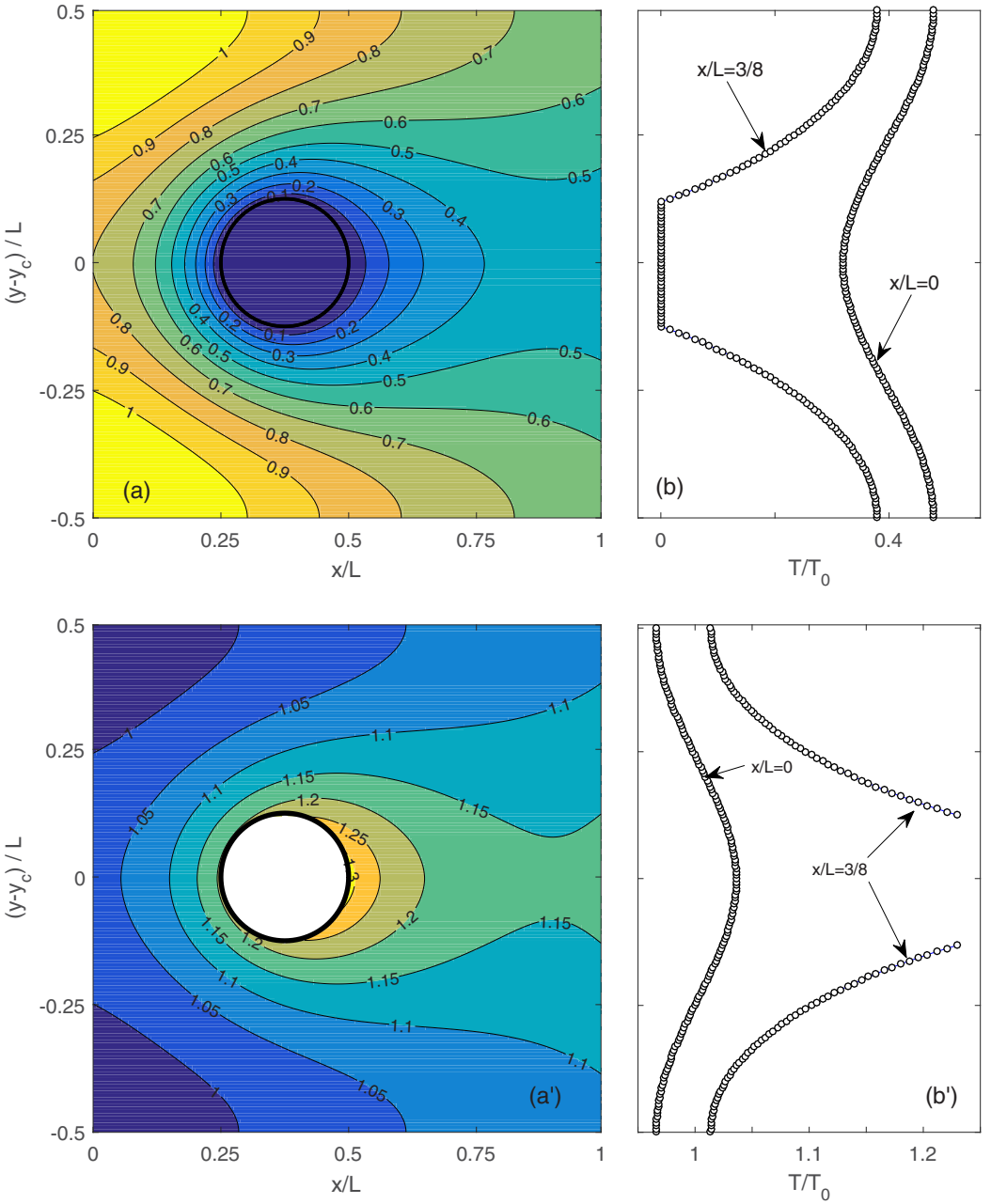

FIG. 9. Result comparison of the simulations for the thermal flows around cylinder using the DM or ST approaches for the [(a) and (b)] CWT and [(a′) and (b′)] SHF wall conditions. In the temperature fields [(a) and (a′)], the color patches are from the DM approach, and the isotherm lines are from the ST approach. The temperature profiles at $x/L = 0$ and $3/8$ (indicated by labels) are displayed in (b) and (b′), with the symbols from the DM approach and curves from the ST approach.

utilized to simulate incompressible periodic thermal flows. The temperature difference seems to vary more smoothly in space for the CWT system than the SHF system; however, the detailed mechanism responsible for this observation is out of the capacity of the authors.

IV. SUMMARY AND CONCLUDING REMARKS

We have examined the periodic relationships in flow and temperature fields for fully developed periodic incompressible thermal flows with CWT and SHF boundary conditions, and proposed two LBM implementations (the ST and DM approaches) for such flow situations. The methods have then been tested carefully in several simulations by comparing our LBM results to those from analytical solutions, previous publications, and our own LBM simulations using different numerical techniques. The good performance suggests that our methods could be useful for future LBM thermal simulations.

Since the purpose of this paper is to propose these LBM methods for periodic thermal flows, we have limited our formulations and demonstrations to 2D, laminar, and steady flow situations. Extending these methods to other LBM models (other lattice structures, three-dimensional, multiple-relaxation-time models, or even turbulent LBM models)

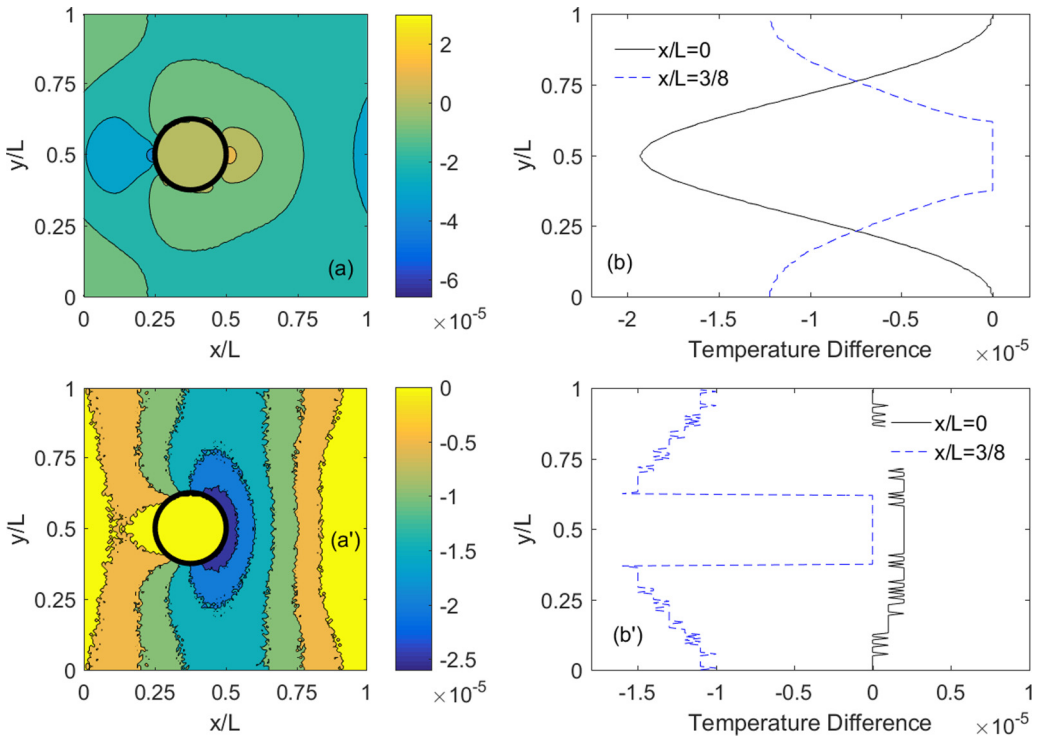

FIG. 10. Distributions of temperature difference between simulations using the ST and DM approaches for the [(a) and (b)] CWT and [(a′) and (b′)] SHF wall conditions. The temperature difference from (a) and (a′) at two representative locations $x/L = 0$ (black solid line) and $3/8$ (blue dashed line) are shown in (c).

should be relatively straightforward. Other alternative thermal LBM models [14,15,17] can also be adopted to solve the thermal field. In addition, although the systems considered in this paper are relatively simple, more complex geometric shapes and boundary conditions (for example, different heat flux magnitudes at different wall locations) can be readily simulated by our methods. For more realistic situations such as unsteady and turbulent periodic thermal flows, some numerical strategies [4,6,31] used in previous computational fluid dynamics (CFD) studies can be considered.

For the two numerical schemes to implement the periodic features of temperature in LBM, the ST approach has been typically used in traditional CFD studies, and certainly can also be adopted in LBM. On the other hand, the DM approach is unique for LBM with some computational advantages. In the DM method, extra calculations are only required for the thermal distributions crossing the periodic inlet/outlet boundaries; but in the ST method, an extra term has to be calculated for all distributions and at all lattice nodes. Furthermore, for systems with CWT boundaries, the ST approach also needs to calculate the streamwise derivative of temperature [$\partial\bar{\theta}/\partial x$ in Eq. (13)], and this could further increase the computational demand. The method in Eq. (16) to calculate the decaying rate λ_L does not require a volumetric integration of temperature over the entire computational domain, and thus it could also be useful for improving the computational efficiency for other CFD methods.

ACKNOWLEDGMENTS

This work was supported by the Natural Science and Engineering Research Council of Canada (NSERC). The calculations have been enabled by the use of computing resources provided by WestGrid (westgrid.ca), SHARCNet (sharcnet.ca), and Compute/Calcul Canada (computecanada.org).

APPENDIX A: DOUBLE-DISTRIBUTION THERMAL LBM MODEL

Here we describe the double-distribution lattice Bhatnagar-Gross-Krook (LBGK) model for thermal flows [32], although other LBM models are available in the literature [14,15,17]. Here two sets of density distribution functions are employed: one as f_i for the fluid dynamics and one as h_i for the thermal convection-diffusion equation. The subscript i denotes the lattice direction in which the distributions f_i or h_i move. The evolution of such density distributions can be described by two consecutive steps: the collision step and the propagation or streaming step. In the collision step, the incoming distributions $f_i(\mathbf{x},t)$ and $h_i(\mathbf{x},t)$, at a lattice node $(\mathbf{x},t)$ ($\mathbf{x}$ as the position vector with two coordinate components x and y) from different directions $i = 0,1,\ldots,b-1$ (b is the total number of lattice velocities of the lattice model employed), mix and then are redistributed into all lattice directions, with mass, momentum, and energy conserved. The new distributions are called postcollision distributions and they are represented as f_i^* and h_i^* in this work. The collision step can be expressed mathematically as

$$f_i^*(\mathbf{x},t) = f_i(\mathbf{x},t) - \frac{1}{\tau_f}\left[f_i(\mathbf{x},t) - f_i^{\mathrm{eq}}(\mathbf{x},t)\right] + \delta f_i, \qquad \text{(A1)}$$

$$h_i^*(\mathbf{x},t) = h_i(\mathbf{x},t) - \frac{1}{\tau_h}\left[h_i(\mathbf{x},t) - h_i^{\mathrm{eq}}(\mathbf{x},t)\right] + \delta h_i. \qquad \text{(A2)}$$

The relaxation parameters τ_f and τ_h are related to the fluid kinematic viscosity ν and thermal diffusivity α, respectively; the additional terms δf_i (usually called the forcing term) and δh_i (usually called the source term) can be tuned to recover the correct macroscopic momentum and energy equations. These issues will be discussed below. The fluid density ρ, equilibrium velocity $\mathbf{u}^{\rm eq}$, and energy scalar A (could be the regular temperature T or its modified counterparts such as $\widetilde{T}$, θ, or $\bar{\theta}$, depending on which energy equation to solve by distributions h_i) can be obtained from the density distributions f_i and h_i as

$$\rho = \sum_i f_i, \quad \mathbf{u}^{\rm eq} = \sum_i f_i \mathbf{c}_i \Big/ \sum_i f_i, \quad A = \sum_i h_i, \tag{A3}$$

where $\mathbf{c}_i$ is the ith lattice velocity. The equilibrium distributions $f_i^{\rm eq}$ and $h_i^{\rm eq}$ can then be calculated from these properties as [14,18,24]

$$f_i^{\rm eq} = \omega_i \rho \left[1 + \frac{\mathbf{c}_i \cdot \mathbf{u}}{c_s^2} + \frac{(\mathbf{c}_i \cdot \mathbf{u})^2}{2c_s^4} - \frac{\mathbf{u}^2}{2c_s^2}\right], \tag{A4}$$

$$h_i^{\rm eq} = \omega_i A \left[1 + \frac{\mathbf{c}_i \cdot \mathbf{u}}{c_s^2} + \frac{(\mathbf{c}_i \cdot \mathbf{u})^2}{2c_s^4} - \frac{\mathbf{u}^2}{2c_s^2}\right]. \tag{A5}$$

The parameter ω_i is called the lattice weight factor and c_s is the lattice sound speed. In the following propagation step, the post-collision distributions f_i^* and h_i^* will then move to the nearest neighboring lattice node at velocity $\mathbf{c}_i$ over a time step δt:

$$f_i(\mathbf{x} + \mathbf{c}_i \delta t, t + \delta t) = f_i^*(\mathbf{x}, t); \tag{A6}$$

$$h_i(\mathbf{x} + \mathbf{c}_i \delta t, t + \delta t) = h_i^*(\mathbf{x}, t). \tag{A7}$$

Now they become the incoming, precollision density distributions at node $\mathbf{x} + \mathbf{c}_i \delta t$, and the above-described collision-propagation process can be repeated iteratively, till satisfactory results have been obtained.

Appropriate mathematical analysis such as the Chapman-Enskog expansion can be performed to the above distribution dynamics, and the following macroscopic equations can be derived [14,15]:

$$\frac{\partial \rho}{\partial t} + \rho \nabla \cdot \mathbf{u} = 0, \tag{A8}$$

$$\frac{\partial \mathbf{u}}{\partial t} + \nabla \cdot (\mathbf{u}\mathbf{u}) = -\frac{\nabla P}{\rho} + \nu \nabla^2 \mathbf{u} + \mathbf{F}, \tag{A9}$$

$$\frac{\partial A}{\partial t} + \mathbf{u} \cdot \nabla A = \alpha \nabla^2 A + S. \tag{A10}$$

The fluid properties $\mathbf{u}$, P, ν, and α are related to the LBM parameters by

$$\mathbf{u} = \mathbf{u}^{\rm eq} + \frac{\mathbf{F}\delta t}{2\rho}, \quad P = c_s^2 \rho, \quad \nu = c_s^2 \left(\tau_f - \frac{1}{2}\right)\delta t,$$

$$\alpha = c_s^2 \left(\tau_h - \frac{1}{2}\right)\delta t. \tag{A11}$$

The additional terms δf_i and δh_i in Eqs. (A1) and (A2) are related, respectively, to the forcing term $\mathbf{F}$ and source term S in the resulting macroscopic Eqs. (A9) and (A10) as

$$\delta f_i = \frac{\omega_i \mathbf{F} \cdot \mathbf{c}_i \delta t}{c_i^2}, \tag{A12}$$

$$\delta h_i = \omega_i S\,. \tag{A13}$$

These δf_i and δh_i terms can be conveniently adjusted according to the forcing or source terms in the macroscopic equations to be solved. In our next validation and demonstration simulation examples, we use the simple D2Q9 (2D and $b = 9$) square lattice structure, for which the nine lattice velocities are

$$\mathbf{c}_0 = \begin{pmatrix} 0 \\ 0 \end{pmatrix}, \quad \mathbf{c}_{1-4} = \begin{bmatrix} \cos(i-1)\pi/2 \\ \sin(i-1)\pi/2 \end{bmatrix} \frac{\delta x}{\delta t},$$

$$\mathbf{c}_{5-8} = \sqrt{2} \begin{bmatrix} \cos(2i-9)\pi/4 \\ \sin(2i-9)\pi/4 \end{bmatrix} \frac{\delta x}{\delta t}. \tag{A14}$$

The lattice weight factors are $\omega_0 = 4/9$, $\omega_{1-4} = 1/9$, and $\omega_{5-8} = 1/36$; and the lattice sound speed $c_s = 1/\sqrt{3}\delta x/\delta t$. δx is the lattice grid resolution.

APPENDIX B: ANALYTICAL SOLUTION FOR DEVELOPED THERMAL FLOW BETWEEN PARALLEL PLATES WITH CONSTANT WALL TEMPERATURE

For a fully developed incompressible flow between two parallel plates of a separation H, the streamwise velocity is

$$u_x(y) = \frac{3}{2} U_0 \left[1 - \left(\frac{2y}{H}\right)^2\right], \tag{B1}$$

and the transverse velocity is $u_y = 0$. Here U_0 is the mean velocity and the transverse coordinate y measures from the centerline at $y = 0$. The two channel walls then locate at $y = \pm H/2$. For the steady thermal flow simulated in Sec. III A, the energy Eq. (3) is simplified to

$$\frac{3}{2} U_0 \left[1 - \left(\frac{2y}{H}\right)^2\right] \frac{\partial T}{\partial x} = \alpha \left(\frac{\partial^2 T}{\partial x^2} + \frac{\partial^2 T}{\partial y^2}\right). \tag{B2}$$

Following Ref. [25], we define the new coordinates as $\bar{y} = 2y/H$ and $\bar{x} = \frac{2x/H}{\rm PrRe'}$, where the Reynolds number is given as ${\rm Re}' = 2U_0 H/\nu$. Please note here the Reynolds number ${\rm Re}'$ is different from the Reynolds number ${\rm Re} = U_0 H/\nu$ used in Sec. III A. The energy equation Eq. (B2) can then be written as

$$\frac{3}{8}(1 - \bar{y}^2) \frac{\partial T}{\partial \bar{x}} = \frac{\partial^2 T}{\partial \bar{y}^2} + \left(\frac{1}{\rm PrRe'}\right)^2 \frac{\partial^2 T}{\partial \bar{x}^2}. \tag{B3}$$

To represent the similar temperature profile along this uniform duct, the temperature field is assumed as a product of a function Y (which only has $\bar{y}$ as the variable) and a decaying function $e^{-8\lambda^2 \bar{x}/3}$ along the flow direction:

$$T(\bar{x}, \bar{y}) = Y(\bar{y}) e^{-\frac{8}{3}\lambda^2 \bar{x}}. \tag{B4}$$

Here the parameter λ is called the eigenvalue and its value will be determined next. For the periodic situation in this study, we are only interested in the first eigenvalue and its corresponding mode, since higher-order modes have disappeared in the developing region due to their faster decaying speed. Equation (B4) is now further simplified to a differential equation of function Y only as

$$Y'' + \left[1 + \left(\frac{8\lambda}{3{\rm PrRe'}}\right)^2\right] \lambda^2 Y - \lambda^2 \bar{y}^2 Y = 0. \tag{B5}$$

Considering the flow and temperature symmetry about the channel centerline at $\bar{y} = 0$, we further express the function Y

as a polynomial series of only even order terms:

$$Y(\bar{y}) = \sum_{i=0}^{\infty} b_i \bar{y}^{2i}. \tag{B6}$$

Submitting this series expression into Eq. (B5) yields the following recursion relationships among the coefficients b_i:

$$b_0 = 1; b_1 = \frac{mb_0}{2}; \quad b_i = \frac{mb_{i-1}+nb_{i-2}}{2(i+1)(2i+1)} \ (i = 2,3,4,\ldots), \tag{B7}$$

with

$$m = -\left[1 + \left(\frac{8\lambda}{3\mathrm{Pr}\,\mathrm{Re}'}\right)^2\right]\lambda^2; n = \lambda^2. \tag{B8}$$

A trial-and-error procedure is required to determine the value λ [25]. Here we start with the value of 1.6815953222 from Ref. [25], and a set of coefficients b_i (up to the 50th term in our calculation) can be calculated from Eq. (B7). The function value of $Y(\bar{y} = 0)$ is then obtained from Eq. (B6), and the difference between $Y(\bar{y} = 0)$ and 0 (the wall temperature requirement) can serve as the criterion to refine the λ value, until a satisfactory resolution is reached. For the system considered in this paper with $\mathrm{Pr} = 0.7$ and $\mathrm{Re} = 40$, the eigenvalue obtained from this trial-and-error process is $\lambda = 1.675516290994$, which is slightly lower than the value from Ref. [25]. The Nusselt number can also be readily calculated from the calculated temperature profile from this λ value, in combination of the parabolic Poiseuille flow velocity Eq. (B1). The analytical Nusselt number is constant along the channel of 3.7723, slightly larger than that in Ref. [25] (3.7704) where axial diffusion is neglected. This is reasonable since the axial diffusion effect enhances the heat transfer efficiency of the system; however with a relatively large Peclet number $\mathrm{Pe} = \mathrm{RePr} = 28$ here, the diffusion contribution to the overall heat transfer is not significant.

[1] J. P. Holman, *Heat Transfer* (McGraw-Hill, New York, 1968).
[2] F. P. Incropera, D. P. DeWitt, T. L. Bergman, and A. S. Lavine, *Fundamentals of Heat and Mass Transfer*, 6th ed. (John Wiley & Sons, New York, 2006).
[3] S. V. Patankar, C. H. Liu, and E. M. Sparrow, ASME J. Heat Transf. **99**, 180 (1977).
[4] M. Greiner, R. J. Faulkner, V. T. Van, H. M. Tufo, and P. F. Fischer, ASME J. Heat Transf. **122**, 653 (2000).
[5] B. Niceno and E. Nobile, Int. J. Heat Fluid Flow **22**, 156 (2001).
[6] E. Stalio and M. Piller, ASME J. Heat Transf. **129**, 769 (2007).
[7] T. Adachi and H. Uehara, Int. J. Heat Mass Transf. **44**, 4333 (2001).
[8] H. M. S. Bahaidarah, N. K. Anand, and H. C. Chen, Num. Heat Transf. A **47**, 417 (2005).
[9] C. Semprebon, T. Kruger, and H. Kusumaatmaja, Phys. Rev. E **93**, 033305 (2016).
[10] X. Yang, H. Huang, and X. Lu, Phys. Rev. E **92**, 063009 (2015).
[11] C. Zhang, Y. Cheng, J. Wu, and W. Diao, J. Hydrodyn. Ser. B **28**, 400 (2016).
[12] J. W. Murraya, J. Sunb, D. V. Patilb, T. A. Woodc, and A. T. Clarea, J. Mater. Process. Technol. **229**, 54 (2016).
[13] J. Wang, Q. Kang, L. Chen, and S. S. Rahman, Int. J. Coal Geol. **169**, 62 (2017).
[14] Z. Guo and C. Shu, *Lattice Boltzmann Method and Its Applications in Engineering* (World Scientific, Singapore, 2013).
[15] S. Succi, *The Lattice Boltzmann Equation* (Oxford University Press, Oxford, 2001).
[16] J. Zhang, Microfluid. Nanofluid. **10**, 1 (2011).
[17] Q. Li, K. Luo, Q. Kang, Y. He, Q. Chen, and Q. Liu, Prog. Energy Combust. Sci. **52**, 62 (2016).
[18] Q. Chen, X. Zhang, and J. Zhang, Commun. Comput. Phys. **17**, 937 (2015).
[19] J. Zhang and D. Y. Kwok, Phys. Rev. E **73**, 047702 (2006).
[20] Y. Han and P. A. Cundal, Int. J. Numer. Meth. Fluids **67**, 1720 (2011).
[21] J. Zhang and D. Y. Kwok, J. Comput. Phys. **206**, 150 (2005).
[22] T. Zhang, B. Shi, Z. Chai, and F. Rong, Commun. Comput. Phys. **11**, 1569 (2012).
[23] X. Yin and J. Zhang, J. Comput. Phys. **231**, 4295 (2012).
[24] Q. Chen, X. Zhang, and J. Zhang, Phys. Rev. E **88**, 033304 (2013).
[25] G. M. Brown, AIChE J. **6**, 179 (1960).
[26] G. Le and J. Zhang, Phys. Rev. E **79**, 026701 (2009).
[27] O. Oulaid and J. Zhang, Eur. J. Mech. B-Fluid **53**, 11 (2015).
[28] A. G. Ramgadia and A. K. Saha, Int. J. Therm. Sci. **67**, 152 (2013).
[29] G. Wang and S. P. Vanka, Int. J. Heat Mass Transf. **38**, 3219 (1995).
[30] O. Oulaid, Q. Chen, and J. Zhang, J. Phys. A **46**, 475501 (2013).
[31] A. K. Saha and S. Acharya, Int. J. Heat Mass Transf. **48**, 4704 (2005).
[32] X. He, S. Chen, and G. D. Doolen, J. Comput. Phys. **146**, 282 (1998).